Spectral index of the Galactic foreground emission in the 50–87 MHz range

M. Spinelli [1,2][★] G. Bernardi,[3,4,5] H. Garsden,[6] L. J. Greenhill,[6] A. Fialkov,[7,8] J. Dowell [9]
and D. C. Price [6,10]

[1]*INAF – Osservatorio Astronomico di Trieste, Via G.B. Tiepolo 11, I-34143 Trieste, Italy*
[2]*IFPU – Institute for Fundamental Physics of the Universe, Via Beirut 2, I-34014 Trieste, Italy*
[3]*INAF – Istituto di Radioastronomia, via Gobetti 101, I-40129, Bologna, Italy*
[4]*Department of Physics and Electronics, Artillery Road, Rhodes University, Grahamstown 6140, South Africa*
[5]*South African Radio Astronomy Observatory, FIR street, Observatory, Cape Town, South Africa*
[6]*Harvard-Smithsonian Center for Astrophysics, 60 Garden Street, Cambridge MA 02138, USA*
[7]*Kavli Institute for Cosmology, Madingley Road, Cambridge CB3 0HA, UK*
[8]*Institute of Astronomy, University of Cambridge, Madingley Road, Cambridge CB3 0HA, UK*
[9]*University of New Mexico, 1919 Lomas Boulevard NE, Albuquerque, NM 87131, USA*
[10]*International Centre for Radio Astronomy Research, Curtin University, Bentley WA 6102, Australia*

ABSTRACT

Total-power radiometry with individual meter-wave antennas is a potentially effective way to study the Cosmic Dawn ($z \sim 20$) through measurement of the sky brightness arising from the 21 cm transition of neutral hydrogen, provided this can be disentangled from much stronger Galactic and extra-galactic foregrounds. In the process, measured spectra of integrated sky brightness temperature can be used to quantify the foreground emission properties. In this work, we analyse a subset of data from the Large-aperture Experiment to Detect the Dark Age (LEDA) in the 50–87 MHz range and constrain the foreground spectral index β in the northern sky visible from mid-latitudes. We focus on two zenith-directed LEDA radiometers and study how estimates of β vary with local sidereal time (LST). We correct for the effect of gain pattern chromaticity and compare estimated absolute temperatures with simulations. We select a reference data set consisting of 14 d of observations in optimal conditions. Using this data set, we find, for one radiometer, that β varies from -2.55 at LST <6 h to a steeper -2.58 at LST ~ 13 h, consistently with sky models and previous southern sky measurements. In the $13 - 24$ h LST range, however, we find that β varies between -2.55 and -2.61 (data scatter ~ 0.01). We observe a similar β versus LST trend for the second radiometer, although with slightly smaller $|\beta|$ over the 24 h, in the $-2.46 < \beta < -2.43$ range (data scatter ~ 0.02). Combining all data gathered during the extended campaign between mid-2018 and mid-2019, and focusing on the LST $= 9-12.5$ h range, we infer good instrument stability and find $-2.56 < \beta < -2.50$ with $0.09 < \Delta\beta < 0.12$.

Key words: instrumentation: miscellaneous – Galaxy: structure – dark ages, reionization, first stars.

1 INTRODUCTION

The challenging measurement of a signal from the Cosmic Dawn of the Universe finds its most promising observable in the 21-cm line of the neutral Hydrogen (e.g. Furlanetto, Oh & Briggs 2006; Pritchard & Loeb 2010). At Cosmic Dawn, Ly-α photons, produced by the first stars, couple the excitation temperature of the 21-cm line to the gas kinetic temperature through the Wouthuysen–Field effect (WF; Wouthuysen 1952; Field 1958), producing a negative contrast against the cosmic microwave background (CMB) temperature and thus an absorption signal. Eventually, the progress of structure formation through gravitational collapse completely couples the spin temperature to the gas temperature. As a consequence of gas heating, most likely by an X-ray background, the gas/spin temperature is then driven well above the CMB temperature (e.g. Venkatesan, Giroux & Shull 2001; Pritchard & Furlanetto 2007; Mesinger, Ferrara &

Spiegel 2013). The interplay between Ly-α coupling and X-ray heating is, thus, expected to create a few hundred mK absorption features in the *global – i.e. sky averaged –* 21-cm signal, sensitive to the formation of the first luminous structures in the Universe (e.g. Barkana & Loeb 2005; Furlanetto et al. 2006; Fialkov et al. 2013; Mirocha 2014; Mesinger, Greig & Sobacchi 2016; Mirocha & Furlanetto 2019), and to the thermal history of the intergalactic medium (Pritchard & Furlanetto 2007; Mesinger et al. 2013; Fialkov, Barkana & Visbal 2014).

In principle, the global 21-cm signal can be measured with a single antenna and noise-switched receiver in $O(10^2)$ h (e.g. Shaver et al. 1999; Bernardi, McQuinn & Greenhill 2015; Harker et al. 2016). The Experiment to Detect the Global Epoch-of-Reionization Signatures (EDGES) team has claimed the detection of a broad absorption profile peaking at -520 mK and centred at 78 MHz (Bowman et al. 2018). This is more than a factor too deeper than predicted from the theory based on standard physics (e.g. Cohen et al. 2017). If the EDGES signal is confirmed to be of cosmological origin, it implies that either the temperature of the radio background is higher than the CMB

(e.g. Bowman et al. 2018) or the neutral gas at $z \sim 17$ is colder than expected (e.g. due to interactions with cold dark matter; Barkana 2018). The flat line profile is also unexpected.

Subsequent analysis by other authors has suggested the existence of a residual unmodelled systematic sinusoidal feature in EDGES data (Hills et al. 2018; Singh & Subrahmanyan 2019; Bevins et al. 2020) that could modify their best-fitting parameters. Similarly, Spinelli, Bernardi & Santos (2019) suggested an unaccounted contamination from polarized foregrounds as a possible explanation. Moreover, using a Bayesian evidence-based comparison, Sims & Pober (2020) found no strong evidence in favour of models including a global 21 cm in the EDGES data. The importance and the implications of the EDGES result need confirmation from another independent experiment to be fully convincing against criticisms.

The effort to measure the global 2-cm signal has been ongoing for several years with variegated instrumental designs. The Large aperture Experiment to detect the Dark Ages (LEDA; Price et al. 2018), whose latest data are analysed in this work, constrained at 95 per cent confidence level the amplitude (>-890 mK) and the 1σ width (>6.5 MHz) of a Gaussian model for the absorption trough (Bernardi et al. 2016). Moreover, the upgraded Shaped Antenna measurement of the background RAdio Spectrum (SARAS 3) has provided constraints in the $6 < z < 10$ range (Singh et al. 2017, 2018); the 'Sonda Cosmologica de las Islas para la Deteccion de Hidrogeno Neutro (SCI-HI; Voytek et al. 2014) reported a 1 K root mean square (rms) residual in the range 60–88 MHz. Other experiments are the Probing Radio Intensity at high-Z from Marion (PRIZM) experiment (Philip et al. 2019), the Broadband Instrument for Global HydrOgen ReioNisation Signal (BIGHORNS; Sokolowski et al. 2015) and the Radio Experiment for the Analysis of Cosmic Hydrogen (REACH).[1] Looking at the future, space experiments orbiting around the Moon (e.g. the Dark Ages Polarimeter Pathfinder [DAPPER][2]) intend to to measure the 21-cm global signal in an environment free of terrestrial radio frequency interference, ionospheric corruptions and solar radio emissions.

The key challenge to measure the 21-cm signal is the subtraction of the bright foregrounds. The low-frequency radio sky is a superposition of several components including galactic synchrotron, free–free emission, supernova remnants, radio galaxies, and absorption from H II regions. Galactic and extra-galactic synchrotron and free–free emissions have a typical sky temperature of thousands of Kelvins at 75 MHz, several orders of magnitude stronger than the pristine Cosmic Dawn signal. The proper characterization of the foreground emission, thus, plays a fundamental role in the 21-cm global signal analysis. Current modelling often uses extrapolations of the all-sky 408-MHz survey (Haslam et al. 1982) to lower frequencies. Other more sophisticated models are available: an improved version of the Global Sky Model (GSM; De Oliveira-Costa et al. 2008; Zheng et al. 2016), including Parkes telescope maps at 150 and 85 MHz (Landecker & Wielebinski 1970), and the Global MOdel for the radio Sky Spectrum (GMOSS; Sathyanarayana Rao et al. 2017) for the 22 MHz–23 GHz range. However, the majority of the information contained in these models is derived at high frequencies. Other measurements are available: Guzmán et al. (2011) produced a Galactic large-scale temperature map at 45 MHz covering more than 95 per cent of the sky and the Northern hemisphere has been covered by the Long Wavelength Array (LWA)-1 Low-Frequency Sky Survey (Dowell et al. 2017) at a range of frequencies between

35 and 80 MHz with few degree resolution. These maps are not in complete agreement with the GSM at the same frequencies, probably due to an increased contribution of free–free absorption (Dowell et al. 2017). Eastwood et al. (2018) released low-frequency maps of the full sky visible from the Owens Valley Radio Observatory (OVRO) between $\sim$36 and $\sim$73 MHz. The OVRO-LWA maps have a 15 arcmin angular resolution, complementing the existing full-sky maps at these frequencies, but being interferometric observations, they do not include the averaged sky brightness.

Global signal experiments, while targeting the Cosmic Dawn, can contribute to the knowledge of the low-frequency radio sky: with their large beams, they average the absolute sky brightness temperature over large spatial scales. Diffuse and continuum foreground sources are known to be spectrally smooth; that is, they should exhibit power-law spectra[3] over the low-frequency band of interest. Measurements of the Galactic foreground spectral index β have been obtained with single dipole antennas. Rogers & Bowman (2008) found that the spectral index of diffuse emission in the frequency range 100–200 MHz is $\beta = -2.5 \pm 0.1$ at high-Galactic latitudes. Patra et al. (2015), using the SARAS experiment, measured the spectral index in the 110–170 MHz band covering the $23 - 1$ h LST range. They reported a slow variation with LST and a steepening from -2.3 to -2.45 when observing off the Galactic Centre. In Mozdzen et al. (2017), the EDGES team obtained a measurement of the spectral index in the Southern hemisphere in the 90–190 MHz frequency range. They found $-2.60 > \beta > -2.62$ in the 0–12 h LST range, increasing up to $\beta = -2.50$ at 17.7 h, when the Galactic Centre is transiting. In the 50–100 MHz range, Mozdzen et al. (2019) found the spectral index to be $-2.59 < \beta < -2.54$ for LST values below 12 h, flattening to -2.46 when the Galactic Centre transits. Moreover, exploiting a lunar occultation technique with the Murchison Widefield Array telescope, McKinley et al. (2018) measured a spectral index of -2.64 ± 0.14, at the position of the Moon, in the frequency range $72-230$ MHz.

The LEDA experiment covers the full Northern hemisphere, offering an important complementary measure of the spectral index. Price et al. (2018), using LEDA data from 40 to 83 MHz, found that the spectral index varies between -2.28 and -2.38 over the full LST range.

In this work, we present new results on the spectral index of the Galactic foreground emission in the 50–87 MHz range using the latest LEDA measurements, covering $\sim$140 nights distributed between mid-2018 and mid-2019.

This paper is organized as follows. In Section 2, we describe the LEDA observations, data processing, and assess the quality of our data. In Section 3.3, we present our beam model and correct for the effect of its chromatic response. This is an important step in order to correctly measure the spectral index and was not performed in previous analyses of LEDA data. In Section 4, we apply a global temperature scale correction to the data to overcome some systematic effects and to match our spectra with the expected sky temperature. Our results are presented in Section 5, followed by discussion and conclusions in Section 6.
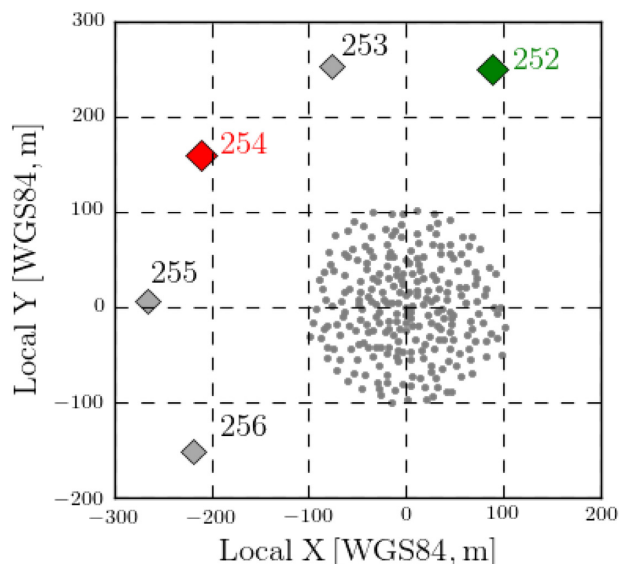
2 OBSERVATIONS AND DATA PROCESSING

Detailed descriptions of LEDA systems can be found in Kocz et al. (2015) and Price et al. (2018). We summarize here the relevant details and describe significant changes to the system made after Price et al.

---

[1] http://www.astro.phy.cam.ac.uk/research/research-projects/reach
[2] https://www.colorado.edu/project/dark-ages-polarimeter-pathfinder

[3] $T(\nu) \propto \nu^{\beta}$

Figure 1. OVRO-LWA antenna positions in WGS84 coordinates relative to the centre, as built in 2013. Diamonds represent LEDA antennas equipped for radiometry. They are well-separated from the core of the array so as to limit mutual coupling effects. We highlight in colour the two antennas whose data are used in this analysis.

(2018). LEDA dual polarization radiometric receivers were installed in place of LWA receivers on a subset of antennas within the OVRO-LWA array (37°14′23″.1998 N, 118°16′53″.9995 W). These 'LEDA antennas' lie in an arc and are ∼170 m away from others (∼42 λ at 75 MHz), so as to limit mutual coupling effects to < 1 per cent in antenna impedance. The array layout is shown in Fig. 1. Each dual-polarization antenna comprises two pairs of triangular dipole arms 1.50-m long, angled downward by 45°. A ∼3.1-cm transmission line connects each antenna terminal to the receiver balun input. The receiver occupies a two-sided ∼13 × 13 cm² circuit board. A separate daughter board carries those voltage regulators that dissipate away the most heat (Price et al. 2018). All components above the dipole arms fit within an uninsulated PVC cubic cover affording 14 × 14 × 11.4 cm3 of space for hardware. The orientation of the east–west dipole axis defines polarization A and the other polarization B. In this analysis, we report on results using polarization A from antennas 252 and 254.

The ground within 3–4 m of each antenna was devoid of vegetation and flatter than that for other LEDA antennas (i.e. undulations ≪±10 cm). Ground screens at each antenna ensured the gain pattern is zenith directed with nulls at the horizon.

Antenna 254 was equipped with a 3 × 3 m² ground screen, comprising a 12.5-mm gauge welded galvanized wire with a 10.2-cm spacing. This was the default for the OVRO LWA station (Paravastu et al. 2007; Schmitt et al. 2009). Through the end of 2019 January, the same applied to antenna 252. Afterwards, the small screen was replaced by a 20 × 20 m² ground screen, comprised of an 11-mm gauge mesh arranged in a 10-m square with serrations created by four 5 m-long isosceles triangles on each side. This rework also enabled manual leveling of the ground around antenna 252 to achieve peak-to-peak variations of ±3 cm. Serrations on the east and west edges were completed in early February, and on the north and south edges in early April (see Fig. 2). In general, serrations are used in antenna design to attenuate the otherwise reinforcing effects of reflections due to the impedance mismatch between the ground and the screen along rectangular edges (e.g. Bowman et al. 2018).

New receiver filters were also installed in order to extend the useful band up to 87.5 MHz.

Observations span a total of 137 d, with 120 d distributed from 2018 December to 2019 May, and 17 d in 2018 May as a further control sample for data stability with time.

In Fig. 3 we report, for illustrative purposes, the distribution of the 137 d across the year, together LST values corresponding to sunrise and sunset. Note that the primary LEDA observational window is during night-time hours. The Sun is a potential source of interference, especially during flare events, and the RFI environment is known to be more quiet at night. Moreover, air traffic and human activity on site is prevalent during daylight hours.

Data were collected with a 24-kHz frequency resolution, over the 30–87.5 MHz range, and radio frequency interference was excised with an iterative thresholding method (Offringa et al. 2010; Price et al. 2018). Calibration was carried out via a three-position switch which loops between the sky, a cold, and a hot load every 5 s, for an actual 30 per cent time duty cycle on the sky. A typical ambient temperature variation may induce up to a 0.2 per cent power change at the receiver output. Spectra were further corrected for reflection coefficients measured in the lab (Price et al. 2018).

As we will discuss further in Section 4, the Galactic plane contributes significantly to the overall system temperature of zenith-directed low-frequency radiometers, so, for aiming at a detection of the 21-cm signal, it is better to observe when the brightest portions of the plane are at low elevations. Fig. 3 displays the preferred LST range for our analysis, which combines night time across all the observing period when the Galactic plane contribution is at minimum.

The consistency of low-frequency radiometer performance depends in part on the environment, the effect of variable soil moisture on complex permittivity being prominent. Seasonal dry conditions in 2018 carrying over from summer persisted into the first half of 2019 January. Consequently, we anticipate data acquired in 2018 December and 2019 January to be the best. This constitutes our *reference* data set. Unusually, heavy winter rains thereafter posed challenges to be addressed in later sections. For the purposes of a more complete analysis of the foreground spectral index, we extend the analysis of December/January data to nearly 24 h (i.e. including sidereal times when bright Galactic emission is high in the sky).

The inclusion of daytime data allows us to consistently analyse a longer LST range with optimal dry soil conditions. Daytime spectra do not show noticeable spectral variations that can be attributed to solar activity. We estimate the contribution of the quiet sun at transit in December/January using the solar model from Benz (2009) and find it to be rather smooth in frequency, with a maximum value of ∼35 K at 80 MHz – i.e. a ∼ 1 per cent contribution to the total sky temperature. According to the Learmonth Solar Radio Spectrograph[4] monitoring, the Sun was essentially quiet during our campaign.

### 2.1 Statistics of data integration and noise levels

At frequencies below ∼50 MHz, where the wavelength is twice the size of the default 3 × 3 m² ground screen configuration, spectra change noticeably over time-scales of a few days, likely due to the instrument sensitivity to environmental effects. We therefore discarded data below 50 MHz, retaining 1540 of the original 2400 channels.

For a single frequency channel, the measured temperature varies over time and includes random Gaussian noise, $T(t) + n$. Assuming

---

[4] https://www.sws.bom.gov.au/

Figure 2. LEDA antenna 254, which sits in a slight depression surrounded by ∼1 m-high woody vegetation (top left-hand panel), 252 prior to January 2019 (top right-hand panel), and 252 after (bottom) completion of the serrated ground screen in early 2019 April. Serrations that most strongly affect data were completed in February. The smaller ground screen (top figures) is $3 \times 3\,\mathrm{m}^2$ (white boundary lines are intended to guide the eye) and flat to 10 cm peak to peak. The larger ground plane (bottom) is $20 \times 20\,\mathrm{m}^2$ tip to tip and flat to 3 cm peak to peak. The antenna structure is aligned to within $1°$ of true north and the antenna mast stands within $1°$ of vertical. At antenna 252 (top right-hand panel), PVC pipes were used as a cattle guard in place of wood fencing because water absorbed from rainfall by the wood has the potential to affect the antenna gain response.
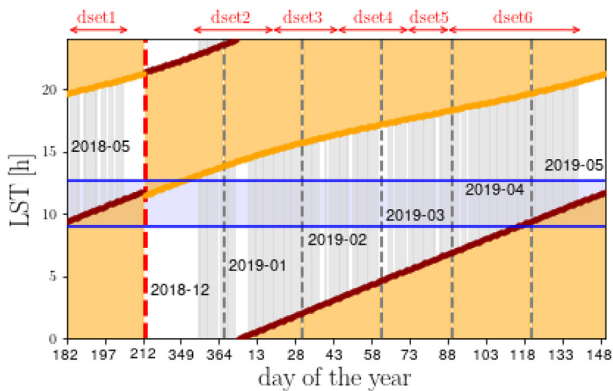

Figure 3. The distribution of the 137 nights analysed in this work between 2018 May and 2019 May (grey vertical solid lines). The yellow band indicates daylight, defined between sunrise (orange line) and sunset (dark red line). Dashed vertical lines divide the months. Note that there is a gap between 2018 May and December highlighted with a red, dashed vertical line. The horizontal blue strip highlights the ∼4-h LST range that is the main focus of our analysis. We anticipate the partition in six *data sets* discussed in Section 2.2 and Fig. 4 at the top margin of the figure.

the noise in each channel to be distributed as a Gaussian with mean $\mu_n = 0$ and standard deviation σ_n, it is possible to estimate the noise variance by removing $T(t)$. This subtraction was performed by de-trending the signal using a mean filter with a sliding-window of ∼4-min width (16 data points). This procedure does not inject correlation into the data, but the uncertainties will be partially correlated over the 4-min interval. Once $T(t)$ is removed, we verify that the extracted noise is Gaussian distributed and estimate the variance σ_n of the distribution. In the range of frequencies used in our analysis, the σ_n values per channel are of the order of tens of Kelvin.

We averaged the signal over 1 MHz-wide channels, using the variance computed in each channel as a weight. The typical noise in a 1-MHz channel is a few Kelvin at 75 MHz for a 5-s integration time. These 1-MHz spectra are the ones used in our analysis.

2.2 Stability and consistence

The observed temperature varies as a function of LST since the foreground sky changes while observed by a fixed antenna, however, it is ideally the same if measured at the same LST over different days. Fig. 4 shows how the observed temperature varies over the course of our observations. For each frequency channel, we plot the relative variation of the observed temperature, calculated against the time
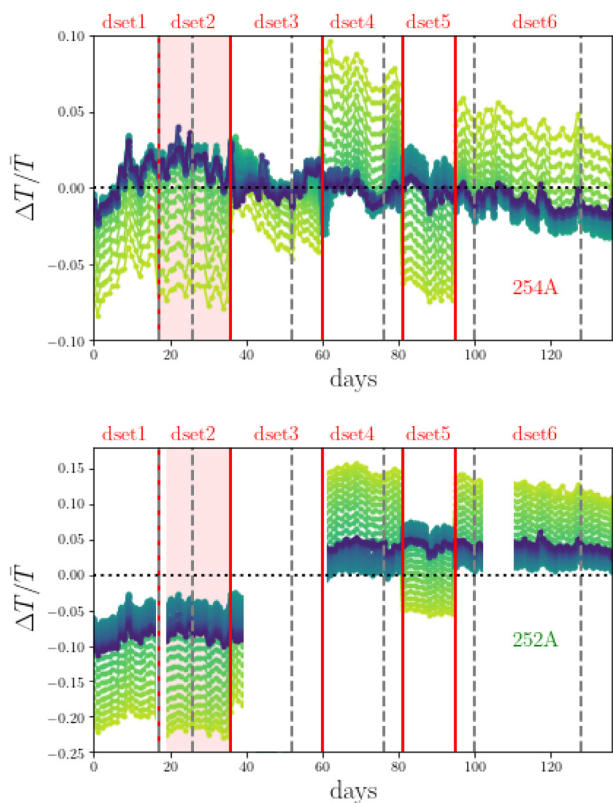
Figure 4. Variations of the measured sky temperature $T_d(\nu)$, for 1-h integration time around LST $=12$ h, as a function of observing day (d), for antenna 254A (upper panel) and 252A (lower panel). We plot the relative difference between $T_d(\nu)$ and its mean value $\bar{T}$ (equation 1). Different colours indicate different frequencies: lower (higher) frequencies are shown in lighter greens (darker blues). Dashed vertical lines denote the separation between months. 2018 May appears at the beginning of the x-axis (note the dashed line superimposing with the first red vertical line), followed by 2018 December up to 2019 May. Note that observations do not span all days of every month, therefore the number of days between two consecutive vertical dashed lines is smaller than 30. The relative temperature shows time discontinuities common to both antennas, more pronounced at low frequencies. These are highlighted in the plot with red vertical lines and define the six different *data sets*. 2018 December and 2019 January data (dset2), marked as a red shaded region, constitute our *reference* data set as they are optimal in terms of soil condition. Note that, despite a less prominent discontinuity, we keep 2018 May separated from 2018 December 2018.

average over N days

$$\bar{T}(\nu) = \frac{1}{N} \sum_{d=1}^{N} T_d(\nu), \text{ with } N = 137. \quad (1)$$

Temporal variations are frequency-dependent in both antennas, with larger effects at low frequencies. We mark them in the figure with red vertical lines and define in this way six different *data sets*, where the temperature remains fairly constant with time. Despite a less sharp change of trend, we kept the data of 2018 May separated from the ones of 2018 December. We recall that the December/January data are our *reference* data set due to the seasonal optimal conditions for humidity and rainfall. The time discontinuities appear more evident in antenna 252A, although contained at few per cent level, reaching 10–20 per cent only at the lowest frequencies ($\nu < 60$ MHz). In this example, we consider 1-h integration time around LST $= 12$ h as a representative trend visible at other LST values too.
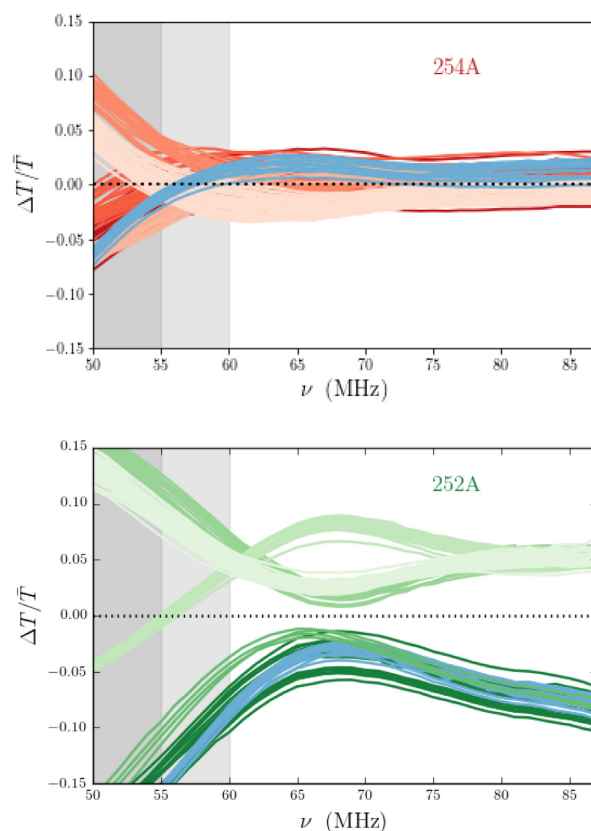

Figure 5. Time variation of sky spectra measured by antenna 254A (upper panel) and 252A (lower panel), plotted as the relative difference with respect the mean value $\bar{T}$ – each colour is a different *data set* as defined in Fig. 4. Chronologically earlier (later) data sets are shown in darker (lighter) colours (red for antenna 254A and green for antenna 252A). The dset2 *reference* data set appears in blue in both plots in order to facilitate its identification. Gray shaded areas identify the lowest frequencies (dark grey $\nu < 55$ MHz, light grey $\nu < 60$ MHz).

We then study the time variation of spectra measured by the two antennas. We show, in Fig. 5, the relative difference with respect to the mean value $\bar{T}$, computed by averaging all measured spectra. We plot the six *data sets* defined above with different colours. The 254A data show good stability: for frequencies higher than 60 MHz, within-data sets and between-data sets differences are at most 5 per cent and do not vary much with frequency. Below 60 MHz, the different trends highlighted in Fig. 4 are again clearly visible, leading up to 10 per cent differences. Antenna 252A has good consistency within each data set, while differences across data sets can be as high as 30 per cent. The latter are due both to temporal offsets as well as low frequency variations, also visible in Fig. 4. Differences are smaller at higher frequencies. We note that antenna 252A has a particularly marked discontinuity between January and February, corresponding to maintenance activities. Further details on the amount of measurements available per LST slot can be found in Appendix A.

3 BEAM CHROMATICITY

The spectral smoothness of the foreground emission is the key property that should allow the retrieval of the 21-cm signal. Regardless of the parametrization used for the foregrounds, a frequency-dependent response of the antenna could corrupt their
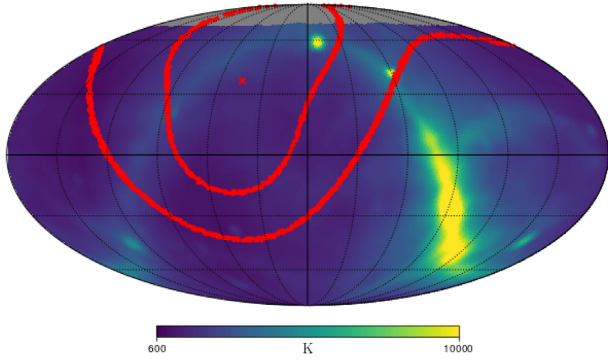
Figure 6. Red contours show –3dB and –10dB projection, in celestial coordinates, of the E–W oriented LEDA antenna model at 75 MHz, for LST =3. The Guzman 45 MHz map scaled at 75 MHz with a constant spectral index of −2.5 is shown in the background for illustration purposes. The grey area shows the missing data at $\rho > 65°$ As the sky drifts the antenna is seeing different structures at the different LSTs.

intrinsic spectra and thus prevent the extraction of the global signal (e.g. Bernardi et al. 2015; Mozdzen et al. 2016; Anstey, de Lera Acedo & Handley 2020; Tauscher, Rapetti & Burns 2020). This beam chromaticity effect, however, can be (at least) partially compensated for by assuming an antenna beam and a foreground model (e.g. Mozdzen et al. 2017, 2019).

3.1 Beam model

We use the NEC-4 package[5] that employs a method of moments to simulate an isolated dipole with a $3 \times 3 \, m^2$ mesh ground screen, a $200 \, \Omega$ load seen by the antenna at its interface with the receiver and a constant soil conductivity of $0.001 \, S \, m^{-1}$. The conductivity value is somewhat more representative of the December/January drier period.

Simulations were used to constrain an analytical beam model (Dowell 2011; Ellingson et al. 2013; Bernardi et al. 2015)

$$B(\nu, \hat{\mathbf{n}}) = \sqrt{[p_E(\theta, \nu) \cos \phi]^2 + [p_H(\theta, \nu) \sin \phi]^2},$$

where $\hat{\mathbf{n}} = (\theta, \phi)$, E and H are the two orthogonal polarizations of the dipole and

$$p_i(\nu, \theta) = \left[1 - \left(\frac{\theta}{\pi/2}\right)^{\alpha_i(\nu)}\right] (\cos \theta)^{\beta_i(\nu)} + \gamma_i(\nu) \left(\frac{\theta}{\pi/2}\right) (\cos \theta)^{\delta_i(\nu)},$$

(2)

with $i = E, H$. The value of the coefficients $[\alpha_i, \beta_i, \gamma_i, \delta_i]$ are fitted with an 11th order polynomial. A projection of the resulting beam in celestial coordinates can be found in Fig. 6.

In order to show the shape of the beam and its frequency structure, we report in Fig. 7 the beam derivative with respect to frequency versus zenith angle θ, for different values of the Azimut angle ϕ, as in Mozdzen et al. (2016). The absolute value of the derivative increases with frequency as expected from the increased chromaticity and the increasingly complex antenna pattern in the direction perpendicular to the main axis. Nevertheless, the pattern does not show rapid variations, ensuring beam smoothness.
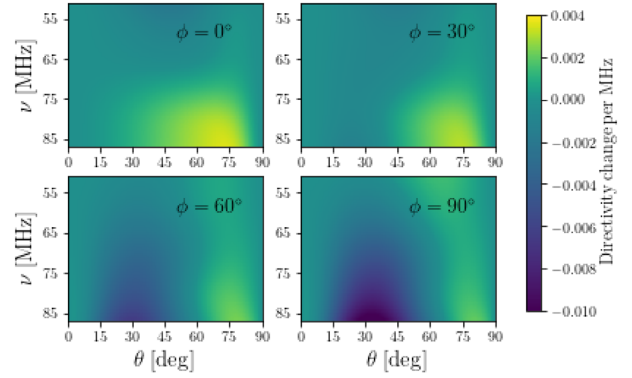
Figure 7. Beam directivity change with respect to frequency (considering 1 MHz steps) at $\phi = 0°$ (E-plane) and $90°$ (H-plane). For completeness, we show also the values for $\phi = 30°$ and $60°$. The horizon response is at $\theta \sim 90°$.

3.2 Foreground model

We first consider the Haslam 408 MHz sky map $T_H(\hat{\mathbf{n}})$ (Haslam et al. 1982) to model foregrounds and scale it to any frequency ν with a constant spectral index across the entire sky, after subtracting the CMB temperature ($T_{cmb} = 2.725$ K)

$$T_{sky}^H(\nu, \hat{\mathbf{n}}) = [T_H(\hat{\mathbf{n}}) - T_{cmb}] \left(\frac{\nu}{408}\right)^{-2.5} + T_{cmb}.$$

(3)

A second foreground model is derived from the 45 MHz Guzman sky map $T_G(\hat{\mathbf{n}})$ (Guzmán et al. 2011). As this map misses data at declination $\delta > 65°$, we inpaint this empty region using $T_{sky}^H(\nu_{45}, \hat{\mathbf{n}})$. We call the resulting map $\tilde{T}_G(\hat{\mathbf{n}})$. We can compute from the Haslam and (inpainted) Guzman maps a more accurate 'wide-band' spectral index $\beta_{GH}(\hat{\mathbf{n}})$

$$\beta_{GH}(\hat{\mathbf{n}}) = \ln \frac{\tilde{T}^G(\hat{\mathbf{n}})}{T^H(\hat{\mathbf{n}})} \left(\ln \frac{45}{408}\right)^{-1}.$$

(4)

The final sky model is constructed similarly to equation 3[6]

$$T_{sky}^G(\nu, \hat{\mathbf{n}}) = [\tilde{T}_G(\hat{\mathbf{n}}) - T_{cmb}] \left(\frac{\nu}{45}\right)^{\beta_{GH}(\hat{\mathbf{n}})} + T_{cmb}.$$

(5)

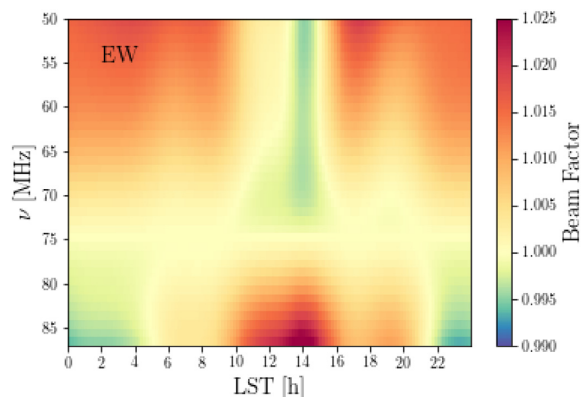### 3.3 Beam chromaticity correction

The beam chromaticity correction can be computed as

$$B_c(\nu, \text{LST}) = \frac{\int_\Omega T_{sky}(\nu_0, \text{LST}, \hat{\mathbf{n}}') B(\nu, \hat{\mathbf{n}}') d\hat{\mathbf{n}}'}{\int_\Omega T_{sky}(\nu_0, \text{LST}, \hat{\mathbf{n}}') B(\nu_0, \hat{\mathbf{n}}') d\hat{\mathbf{n}}'}.$$

(6)

Note that T_{sky} is a function of LST since the sky drifts with time over the antenna. We choose $\nu_0 = 75$ MHz for the reference frequency in order to compare our results with Mozdzen et al. (2019). Note that this is a reasonable choice for us regardless, since it is a quite central frequency for the range of our data. We compute the beam chromaticity using our beam model (Section 3.1) and both the sky model of equations 3 and 5. We find very similar results, differing almost everywhere by less than a few tenths of a per cent. The disagreement is slightly more pronounced closer to the Galactic

Figure 8. Beam chromaticity correction for a simulated E–W oriented LEDA antenna (pol A) as a function of frequency and LST. See text for details.

Centre direction, but never higher than 1 per cent. To test the impact of limitations in our beam model, we instead perturb the coefficients of the beam directivity $p = [\alpha_i, \beta_i, \gamma_i, \delta_i]$ (see equation 2) by drawing values from a Gaussian distribution with standard deviation corresponding to $\sigma_p = 1, 5,$ and 10 per cent of the original parameter value (similar to what was done in Bernardi et al. 2015). We construct 100 beam models by varying simultaneously all four p parameters for each σ_p value and compute the chromaticity corrections. We find variations always smaller than 1 per cent even in the worst case scenario of $\sigma_p = 10$ per cent. We anticipate here that they translate in an error on the spectral index estimation that is smaller than the typical error bar due to the variability of our spectra.

In Fig. 8, we present results using our reference beam model and the Haslam sky model to show consistency with fig. 3 of Mozdzen et al. (2019).

For our final analysis, we compute the chromaticity correction using $T_{\rm sky}^{\rm G}$ and for each LST and frequency we use $B_c(\nu, \rm LST)$ to correct our spectra

$$T_c^{\rm obs}(\nu, \rm LST) \equiv T^{\rm obs}(\nu, \rm LST)/B_c(\nu, \rm LST). \tag{7}$$

4 ABSOLUTE TEMPERATURE SCALE

We investigate the behaviour of the chromaticity corrected spectra $T_c^{\rm obs}(\nu, \rm LST)$ as a function of LST, over the 24-h range (Figs 9 and 10). We focus on the *reference* data set defined in Section 2 and Fig. 4.[7] The measured sky temperature is consistent for the two antennas: it has a minimum in the LST range 10–12 h and reaches its peak around LST ∼18 h, when the Galactic Centre is close to transit.

We compare our results against existing foreground models and measurements by evaluating a simulated antenna temperature

$$T^{\rm ant}(\nu, \rm LST) = \frac{\int_\Omega T_{\rm sky}(\nu, \rm LST, \hat{\mathbf{n}}) B(\nu_0, \hat{\mathbf{n}}) d\hat{\mathbf{n}}}{\int_\Omega B(\nu_0, \hat{\mathbf{n}}) d\hat{\mathbf{n}}}, \tag{8}$$

where $T_{\rm sky}$ are, alternatively LWA1 Low Frequency Sky Survey results (Dowell et al. 2017), the Haslam sky model, $T_{\rm sky}^{\rm H}$ (equation 3), or the Guzman sky model, $T_{\rm sky}^{\rm G}$ (equation 5). Note that we use the beam pattern at the reference frequency $\nu_0 = 75$ MHz in order to avoid the introduction of chromaticity effects.

---

[7]As discussed in Appendix A, when extended to the 24-h range, few days of the *reference* data set have been discarded.
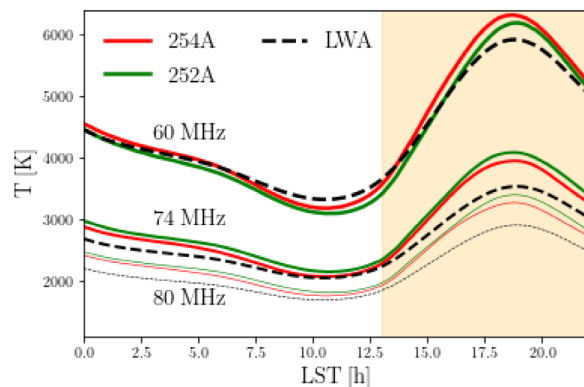

Figure 9. Comparison between the *reference* data set mean sky temperature as a function of LST (antenna 254A in red and 252A green) with the average values of the LWA maps from Dowell et al. (2017) weighted by antenna response (equation 8) at 60, 74, and 80 MHz (black dashed lines with decreasing thickness). For illustrative purposes, the light yellow shaded area indicates the daylight time for LEDA observations, starting approximately at sunrise.
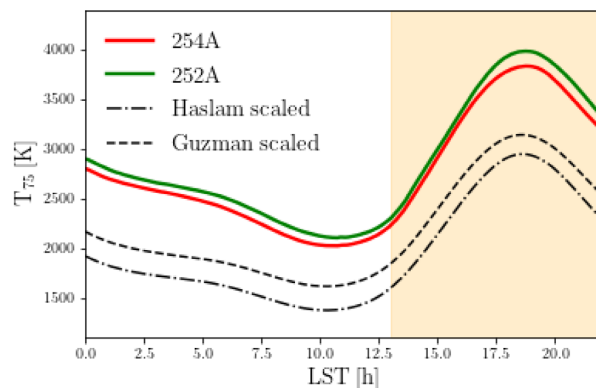
Figure 10. The averaged sky temperature measured by the antennas 254A (red) and 252A (green) at 75 MHz as a function of LST for the *reference* data set. For illustrative purposes, the light yellow shaded area indicates the daylight time for LEDA observations, starting approximately at sunrise. In the figure, we also report the expected behaviour of the mean beam weighted sky temperature (equation 8) at 75 MHz from other existing measurements: the black dot–dash line is obtained with the extrapolated Haslam sky model $T_{\rm sky}^{\rm H}$ (equation 3) and the black dashed from the extrapolated Guzman sky model $T_{\rm sky}^{\rm G}$ (equation 5).

Dowell et al. (2017) have corrected their LWA interferometric observations with the sky-averaged temperature measured in 2014 December by the LEDA prototype system, LEDA-64 New Mexico deployment (Taylor et al. 2012; Schinzel et al. 2018). In Fig. 9, we report the 60, 74, and 80 MHz frequencies and compare with our chromaticity corrected measurements of the sky temperature obtained with antenna 254A and 252A. Their trend with LST is very similar and absolute values are consistent within ∼15 per cent.

In Fig. 10, we compare our measured temperature at 75 MHz for both antennas against the simulated temperature $T^{\rm ant}(75$ MHz, LST) (equation 8), where we use either the Haslam sky model $T_{\rm sky}^{\rm H}$ or the Guzman sky model $T_{\rm sky}^{\rm G}$. Predictions and our measurements have a comparable behaviour with LST, however, they are discrepant in the absolute temperature scale. Although future analysis will be dedicated to investigating the precision of the absolute calibration, in this work, we correct our absolute temperature scale to match the ex-
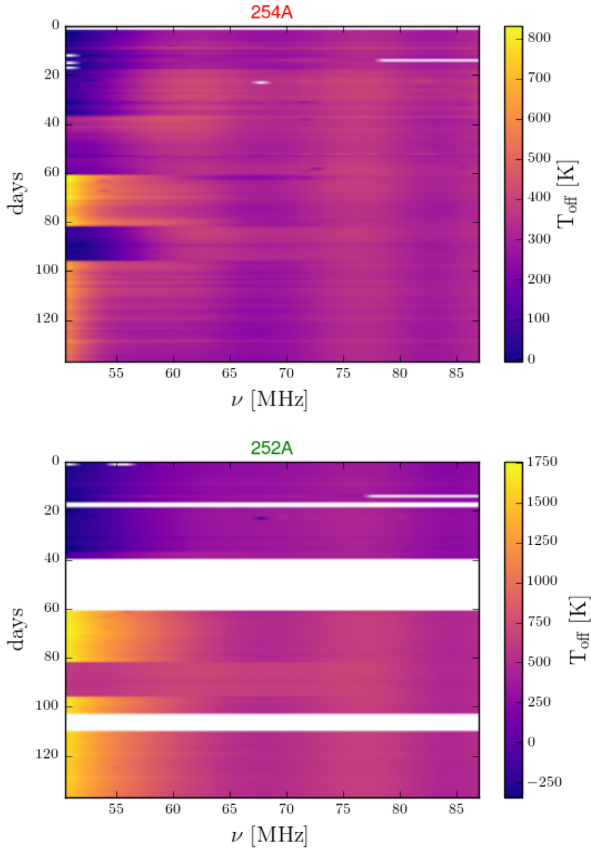
Figure 11. Offset temperature $T_{\rm off}(\nu)$ at LST = 12 h (see equation 9) for antenna 254A (upper panel) and 252A (lower panel) as a function of frequency and observing days. Note that the colour bars have different extents for the two antennas. The difference among *data sets* is particularly evident at low frequency.

trapolation from the 45 MHz map. We make the conservative choice of evaluating $T_{\rm off}$ at LST =12 h, where both the sky temperature and the offset have a minimum. Moreover, the LST = 12 h bin is the only one covered across the whole observing campaign and therefore the most appropriate choice for the correction.

Fig. 11 shows $T_{\rm off}(\nu)$, i.e the difference between all our spectra (corrected for the chromaticity factor) and $T_{\rm sky}^{G}$ at LST = 12 h

$$T_{\rm off}(\nu) \equiv T_c^{\rm obs}(\nu, {\rm LST} = 12{\rm h}) - T_{\rm sky}^{G}(\nu, {\rm LST} = 12{\rm h}). \qquad (9)$$

The offset is relatively constant with frequency and observing day. The strongest differences at low frequencies highlight the different *data sets* defined in Fig. 4. An oscillatory pattern in $T_{\rm off}(\nu)$ with a period of approximately 20 MHz, common to both antennas, and visible across all the observations, can be tentatively inferred from Fig. 11, indicating a possible systematic effect still present in the data.

Offset values for antenna 254A closely follow a Gaussian distribution for each *data set*, and the standard deviation becomes smaller if we restrict the range to 60−87 MHz.

The offset values for antenna 252A span a larger range, as can be seen also in Fig. 11, and their distribution deviates more significantly from a Gaussian profile. We retain for both antennas only $T_{\rm off}(\nu)$ in the 60−87 MHz range and we fit the various distributions with a Gaussian profile to obtain a mean $\bar{T}_{\rm off}$ and standard deviation value for each *data set*. The best-fitting mean and standard deviation are reported in Fig. 12 for both antennas. The results for antenna 254A
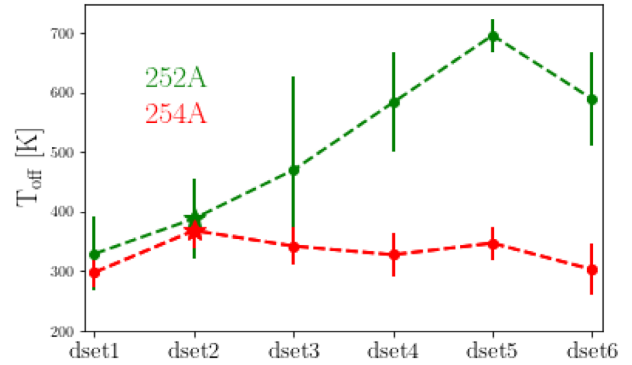
Figure 12. Mean values and 1σ errors obtained from a Gaussian fit of the $T_{\rm off}$ distributions (Fig. 11). The *reference* data set is marked with a star.

are quite stable along the duration of the observations while 252A shows a change of trend, consistently with what has been seen already in Figs 4 and 5. We correct our spectra by subtracting the mean value $\bar{T}_{\rm off}$ for each *data set*.

5 SPECTRAL INDEX RESULTS

We now analyse our observations to characterize the spectral index of the foreground emission. We focus on our *reference* data set in Section 5.1. We recall that for this data set, the observing conditions are optimal in terms of soil and rainfall. We study the spectral index averaging the spectra (measured in 14 selected days) in LST bins of 5 min and across an LST range of ∼24 h. We concentrate instead on the 9−12.5 h LST range, that corresponds to the minimum of foreground contamination, when studying all six *data sets* in Section 5.2. Note that this LST range is the central interval of interest for further studies aimed at extracting a global signal constraint/upper limit. We model the data with a simple power law. Following Mozdzen et al. (2019), we write

$$T_{\rm m}(\nu; \beta, {\rm T}_{75}) = {\rm T}_{75} \left(\frac{\nu}{\nu_{75}} \right)^{\beta} + T_{\rm cmb}, \qquad (10)$$

choosing 75 MHz as a reference frequency. We perform a non-linear least squares minimization to constrain the model parameters for each LST bin, using

$$S = \sum_i^{N_f} \frac{[({\rm T}_c^{\rm obs}(\nu_i) - \bar{T}_{\rm off}) - {\rm T}_{\rm m}(\nu_i)]^2}{\sigma_i^2}, \qquad (11)$$

where N_f is the total number of 1 MHz frequency bins, and the errors σ_i correspond to the noise variance estimates discussed in Section 2.1. We recall that $\bar{T}_{\rm off}$ varies across data sets (Fig. 12). In appendix B, we analyse the effect on the fit of the dispersion around this mean.

5.1 Reference data set results

Fig. 13 shows the best-fitting values of the spectral index as a function of LST and observing day.

Only data above $\nu_{\rm min} = 60$ MHz were used in the fit. We refer to appendix B for a discussion on the stability of the results with respect to this choice. We compute the rms of the residuals for each LST bin and for each day, and report their values in the lower panels of Fig. 13. We check for outliers in both β and rms, and mask the corresponding spectra after a visual check. This procedure discards only few spectra.
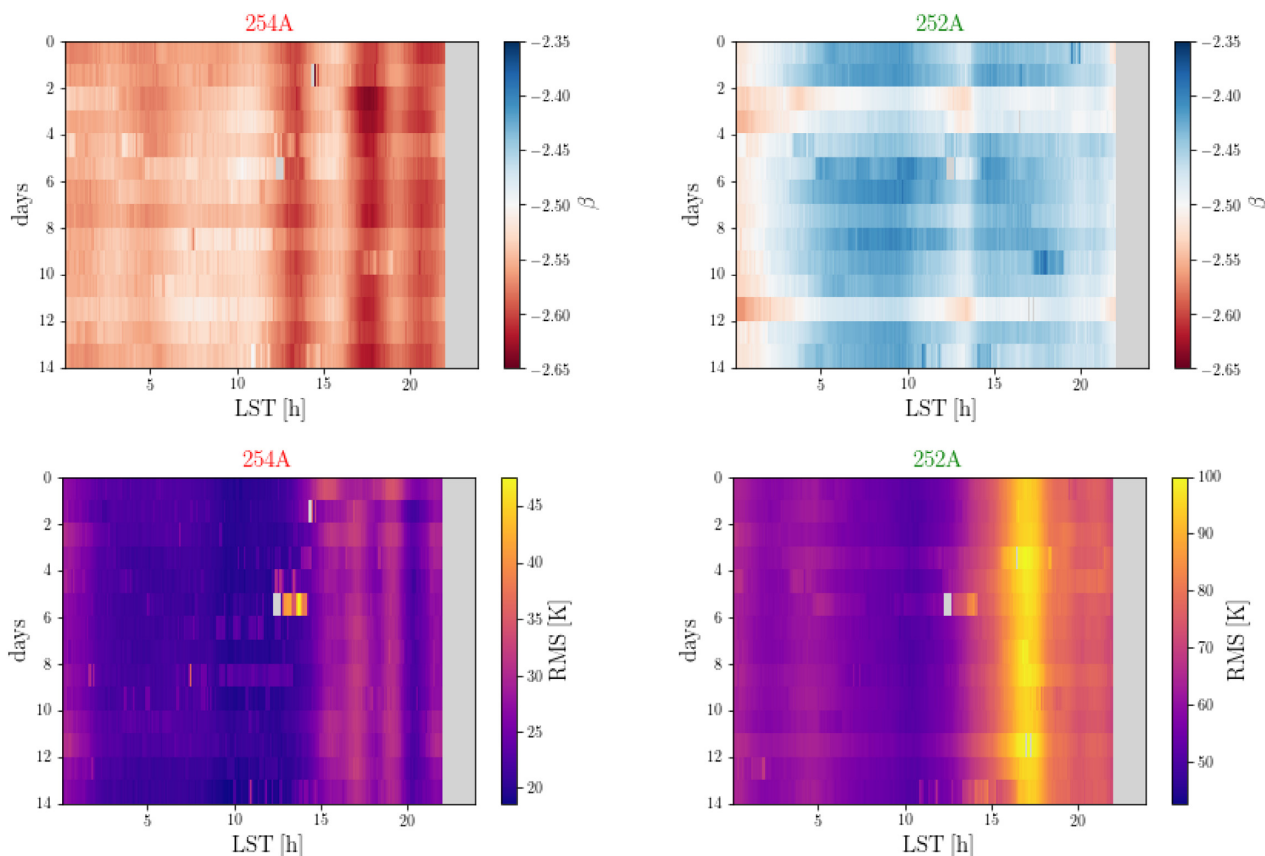
Figure 13. Upper panels: the best-fitting value for the β parameter of equation (10) for our *reference* data set as a function of LST for the antenna 254A (left-hand panel) and 252A (right-hand panel). Note that the colour bar is the same for the two antennas to help the comparison. Lower panels: the rms of the residual spectra for antenna 254A (left-hand panel) and 252A (right-hand panel).

Results are consistent across the observing window, highlighting the good stability of the instrument. The value of the spectral index β steepens around LST ~ 13 h for both antennas. The smallest rms values (around 20 K) occur in the $9-13$ h LST range, motivating further the choice of this interval for further cosmological analysis. Similar trends are found for antenna 252A, although the rms values are overall higher, reaching almost 100 K when the Galactic Centre is in the sky. Note that antenna 254A shows persistent variations at large LST values, in correspondence with high rms values (around 30 K).

We show in the upper panel of Fig. 14 the value of the mean spectral index as a function of LST and its variance across the different days of the data set. The two antennas show similar trends although their results are slightly offset, with antenna 252A pointing towards a flatter β, as visible also from the upper panels of Fig. 13. The mean spectral index shows almost no dependence on LST in the range 0–10 h for antenna 254A and in the range 5–10 h for antenna 252A. It then becomes steeper for both antennas around LST ~ 13 h. Antenna 252A shows an almost constant spectral index for LST > 15 h, while we can recognize the more complex pattern discussed above for antenna 254A. The bottom part of the figure shows that the relative variation between the two antennas that is always lower than 6 per cent. We report in Table 1 the mean value of the spectral index and its standard deviation averaged in LST bins of 3 h. We also report the results obtained without the beam factor correction, to assess its impact. The spectral index, in this case, is found to flatten when the sky temperature is minimal, in agreement with the results in Price et al. (2018), for which the beam chromaticity was not taken into account. The effect of the correction is stronger below LST ~ 5 h and around LST ~ 13 h.

The quoted spectral index scatter in Table 1 and in the upper panel of Fig. 14 is derived directly from the standard deviation of the single antenna measured spectra. The data scatter alone is not enough to reconcile the discrepancy between antenna 254A and 252A, possibly due to the presence of a (yet) unknown systematic effect. To take this into account, we consider together the data from the two antennas. The combined result is shown in the lower panel of Fig. 14. Measurements from the two separate antennas have similar trends in LST, implying that the previous considerations remain valid for the combined results. The mean spectral index β, combining the steeper results from antenna 254A and the flatter results from antenna 252A, varies between -2.54 and -2.48. The uncertainty, now computed from the standard deviation of all the spectra, has a magnitude of $\Delta\beta \sim 0.06$ across the full LST range, reaching $\Delta\beta \sim 0.08$ when the Galactic Centre is above the horizon. We compare this result with existing measurements and simulations. Following Mozdzen et al. (2019), we first compute a spectral index from the comparison of the Haslam and the Guzman maps

$$\beta_{\mathrm{GH}}(\mathrm{LST}) = \ln \frac{T^{\mathrm{ant}}(\nu_{45}, \mathrm{LST})}{T^{\mathrm{ant}}(\nu_{408}, \mathrm{LST})} \left(\ln \frac{45}{408} \right)^{-1}, \tag{12}$$

where $T^{\mathrm{ant}}(\nu, \mathrm{LST})$ is the portion of the sky model seen through the beam as the sky drifts over, and thus is a function of LST. Moreover, we consider both the improved version of the GSM (Zheng et al.
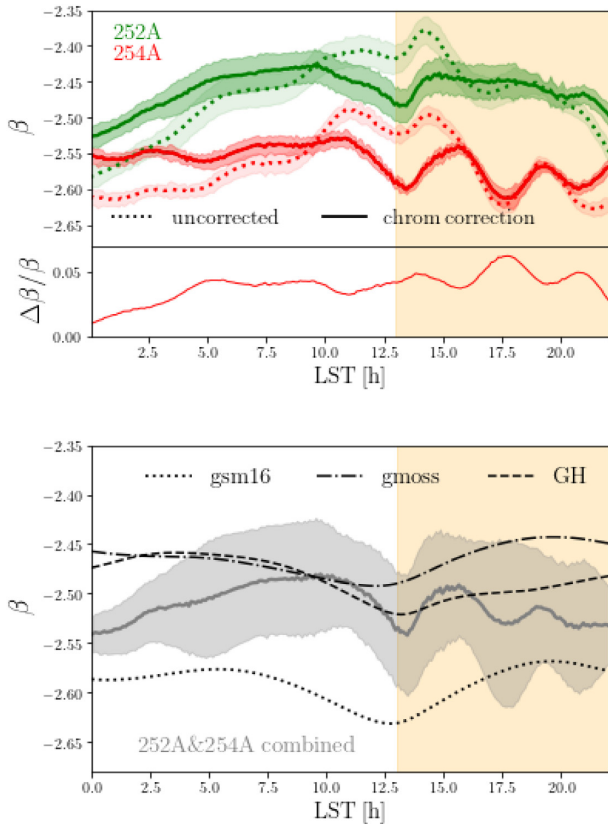
Figure 14. Upper panel: mean value of the best-fitting daily spectral index β, as a function of LST, for the beam corrected reference data set of Fig. 13 (solid lines) compared with the non-corrected one (dotted lines), for the antenna 254A (in red) and 252A (in green). Shaded areas show the standard deviation. The bottom part of the figure shows the relative difference between the result from antenna 252A and 254A. Lower panel: the combined result of both antennas (solid grey line) and relative scatter (shaded area) are compared with the Guzman–Haslam (black dashed), improved GSM (black dotted), and GMOSS (black dashed dotted) spectral indexes (see text for details). For illustrative purposes, the shaded yellow area indicates daylight, starting approximately at sunrise.

Table 1. Spectral index β (equation 10) averaged in 3 h LST bins from the *reference* data set. Errors $\Delta\beta$ are computed from the standard deviation of all the spectra. The rms is also the mean of the rms values within each bin.

LST (h)	254 A β	$\Delta\beta$	rms (K)	252 A β	$\Delta\beta$	rms (K)
0–3	−2.55	0.01	25.08	−2.51	0.02	112.37
3–6	−2.55	0.01	21.99	−2.46	0.02	94.14
6–9	−2.54	0.01	21.90	−2.43	0.02	82.58
9–12	−2.54	0.01	20.70	−2.44	0.02	79.05
12–15	-2.58	0.01	23.31	−2.46	0.02	93.77
15–18	−2.57	0.01	29.33	−2.45	0.02	135.40
18–21	−2.58	0.01	26.96	−2.46	0.02	153.21

2016) and the GMOSS (Sathyanarayana Rao et al. 2017) to create a set of full sky maps in the 60–87 MHz range, with 1 MHz spacing. We then simulate an observation with our antenna beam and consider LST values 10 min apart. We construct a mock spectrum $T^{\rm ant}(\nu,$ LST) for every LST value following this procedure. Note that we consider the beam shape at the reference frequency of 75 MHz to avoid introducing chromaticity effects. We then perform a non-linear

least squares minimization to constrain the model parameters of equation (10) for each LST bin, and report the best-fitting spectral index in Fig. 14.

The LST dependence between models, $\beta_{\rm GH}$ and our observations is in good agreement. Note, for example, the steeper spectral index around LST ~ 13 h. It is worth noticing that the best-fitting values for the scaling temperature T_{75} are well in agreement with their observed ones, once corrected for the offset. This assures that the best-fitting solution is not falling into un-physical minima.

5.2 All data set results

We now analyse the value of the spectra index for the spectra in the six *data sets* defined in Section 2, following the same procedure of Section 5.1. Although the data show a coherent behaviour on a time-scale of few tens of days, there are changes throughout the months that reflect in different $\bar{T}_{\rm off}$ values for each data set. Slight variations across *data sets* are, thus, expected for the best-fitting values of the spectral index.

We display β values as a function of LST and observing day in Fig. 15, and list the mean and standard deviation for each data set in Table 2. We also report the averaged rms values of the residuals. We note that, in the restricted $9-12.5$ h LST range, we can extend the *reference* data set by including more spectra that we otherwise discard over the full 24-h range in order to achieve higher accuracy. For this reason, dset2 has larger error bars than the one presented in Section 5.1.

Fig. 16 displays the mean and standard deviation as a function of LST for each data set, obtained from Fig. 15. There is good consistency across data sets and we find similar variation as a function of LST, in particular, for antenna 254A. We also report the variation of the residual rms in the lower panels. rms values are always lower for antenna 254A than for antenna 252A, as found for the case of the *reference* data set. We do not report the best-fitting value of T_{75} although they are in agreement with the (offset corrected) measured value of the sky temperature at 75 MHz.

Similarly to what was done in Section 5.1, Fig. 17 shows the combined spectral index β and its standard deviation considering both antennas and all *data sets*. The mean value of β varies from a minimum of -2.50 at LST ~ 11 h to a steeper -2.56 at LST ~ 12.5 h. The combined error bar spans the $0.09 < \Delta\beta < 0.12$ range. We compare the result with existing measurements and simulations.

6 DISCUSSION AND CONCLUSIONS

We presented the analysis of LEDA radiometric data with the aim of measuring the spectral index of Galactic radio emission in the 60–87 MHz range. Observations were carried out with two antennas (252A and 254A) and spanned a total of ~ 600 h divided in six different *data sets* taken in 2018 May and from 2018 mid-December to 2019 mid-May.

Observed spectra were corrected for the effect of beam chromaticity following Mozdzen et al. (2017, 2019) and re-scaled to be in agreement with the absolute temperature scale derived from existing observations (Haslam et al. 1982; Guzmán et al. 2011). The beam chromaticity effect leads to spectral index corrections smaller than ~ 4 per cent. We note here that an approach that incorporates beam effects in the foreground model and therefore bypasses the chromaticity correction, has recently been discussed in the literature (Anstey et al. 2020; Tauscher et al. 2020), although not applied to observations yet.
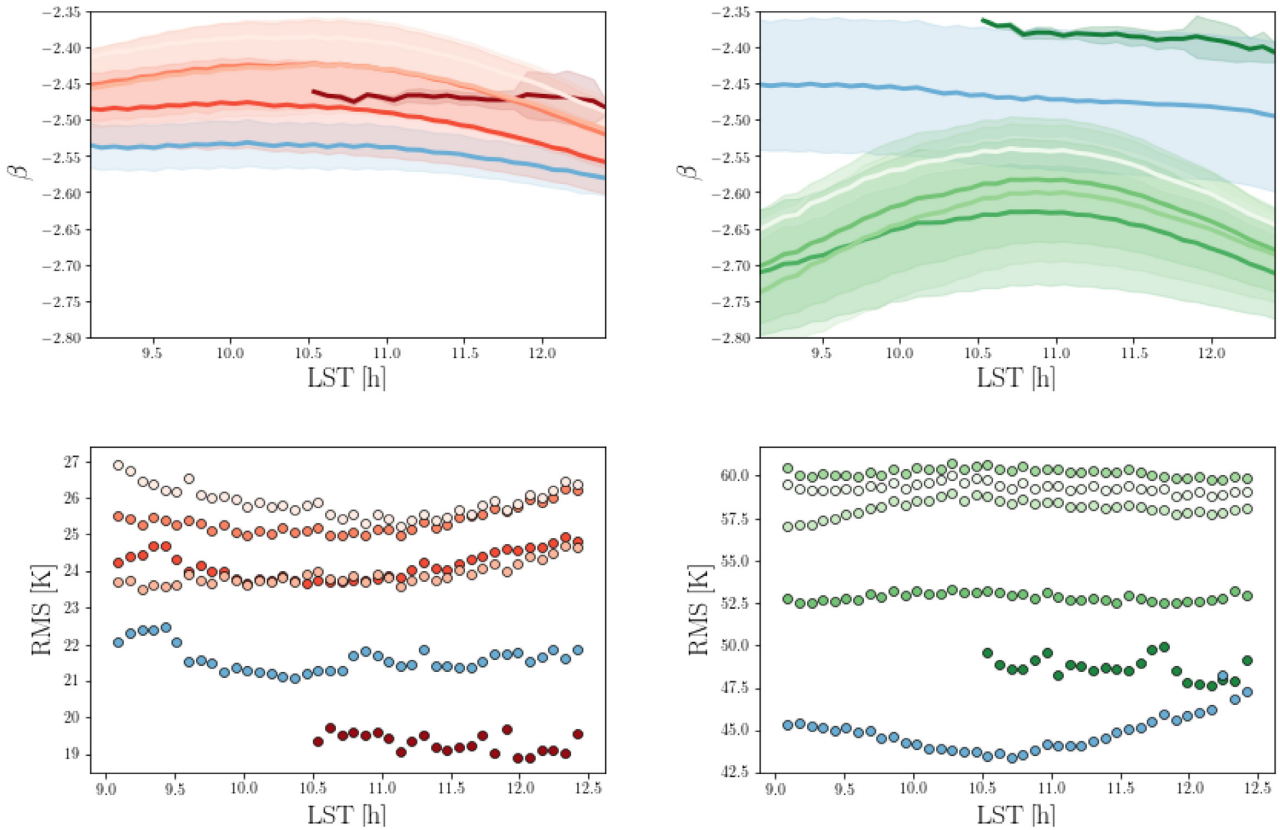
Figure 16. Upper panel: mean and standard deviation of the spectral index the best-fitting values from Fig. 15, split between the different data sets defined in Section 2, for antenna 254A (left-hand panel, red scale) and antenna 252 (right-hand panel, green scale). The colour code is the same as Fig. 5. Lower panel: mean residual rms for antenna 254A (left-hand panel) and 252A (right-hand panel). Every marker represents a different LST bin (~5-min long), colour coded to identify the different data sets. The *reference* data set is reported in blue to facilitate its identification.

Due to optimal soil conditions, we first focused on 14 d of data from 2018 December and early 2019 January (*reference* data set). We found that the spectral index is fairly flat across the 24-h LST range. It varies from $\beta = -2.55 \pm 0.01$ for antenna 254A at LST <6 h to $\beta = -2.58 \pm 0.01$ at LST ~13 h. A similar behaviour is found for antenna 252A, although with a flatter mean, ranging from $\beta = -2.43 \pm 0.02$ to -2.46 ± 0.02. Residual rms values after subtracting the best-fitting power law vary from 20–30 K for antenna 254A to 70–150 K for antenna 252A.

Results from the two antennas show a ~ 5 per cent offset which is larger than their individual uncertainties. We, thus, jointly analyse measurements from the two antennas to account for this systematic offset. The combination of the two antennas leads to values of the spectral index ranging from $\beta = -2.48$ at LST ~10 h to a steeper $\beta = -2.54$ at LST ~13 h, with a typical $\Delta\beta \sim 0.06$ standard deviation.

Our results are broadly consistent with previous measurements. Guzmán et al. (2011) derived a spectral index map between 45 and 408 MHz, where $-2.6 < \beta < -2.5$ over most of the sky. Similarly, Mozdzen et al. (2019) found $-2.59 < \beta < -2.54$ in the $0 < \text{LST} < 12$ h and 50–100 MHz range, flattening to $\beta = -2.46$

when the Galactic Centre is transiting – although their observations cover the southern celestial hemisphere and can, therefore, only be qualitatively compared to ours. We find broad agreement with the Improved GSM (Zheng et al. 2016) and GMOSS (Sathyanarayana Rao et al. 2017) sky models too.

We analysed the full six *data set*s in the $9-12.5$ h LST range, where the foreground temperature shows a minimum. The distribution of the best-fitting spectral index for antenna 254A spans values from -2.54 to -2.41, all consistent with the mean $\beta = -2.48 \pm 0.07$. Spectral indexes are, in general, more variable for antenna 252A, leading to a mean value $\beta = -2.6 \pm 0.1$. The configuration of antenna 252A was not the same throughout the observing period and a larger scatter may be expected in its results. Improved antenna simulations, including a more refined modelling for the ground plane and the soil, are ongoing and will be the subject of a follow-up work.

We combined the six *data sets* from both antennas together and find $\beta = -2.5 \pm 0.1$ in the $9-12.5$ h LST range. The combined mean spectral index value for all our data is in agreement with the result obtained using the *reference* data set (dset2) and consistent with existing sky models.
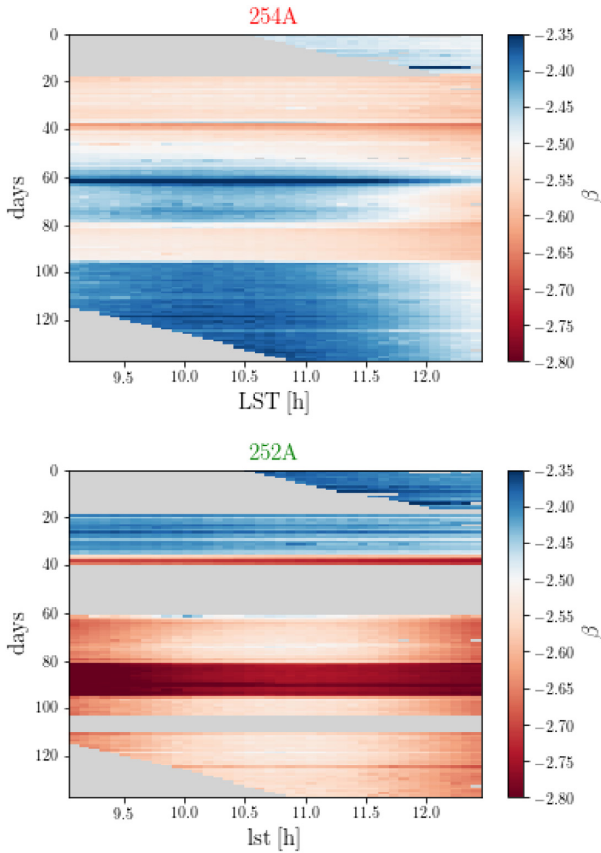
Figure 15. The best-fitting value for the β parameter of equation (10) for every day of our full data set in the LST range 9–12.5 h (LST binning $\sim$ 5 min) for the antenna 254A (upper panel) and 252A (lower panel). Note that data from 2018 May–2019 May do not cover the entire LST range, to avoid data too close to the sunset. The colour bar is the same for the two antennas to aid the comparison.

Table 2. Mean of the best-fitting spectral index β (equation 10) for each of the six *data set*s, obtained by averaging over the $9-12.5$ h LST range. The quoted rms values are averaged accordingly. Errors $\Delta\beta$ are computed from the standard deviation of the spectra.

| Data set | 254 A | | | 252 A | | |
	β	$\Delta\beta$	rms (K)	β	$\Delta\beta$	rms (K)
1	−2.47	0.01	19.32	−2.39	0.01	48.72
2 (ref)	−2.54	0.03	21.60	−2.47	0.10	44.88
3	−2.50	0.06	24.15	−2.66	0.09	52.86
4	−2.44	0.06	25.35	−2.63	0.08	60.20
5	−2.45	0.06	23.90	−2.65	0.09	58.11
6	−2.41	0.02	25.88	−2.58	0.02	59.30
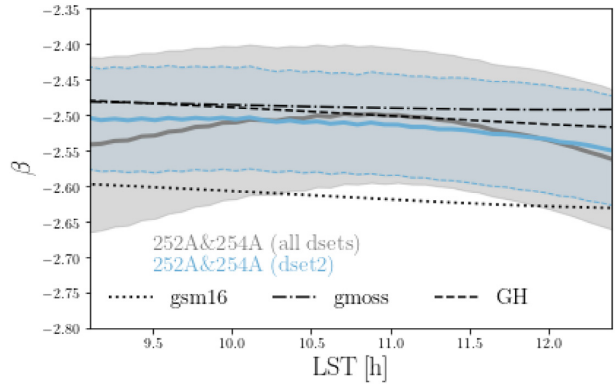
Figure 17. Spectral index as a function of LST obtained by combining all *data sets* and antennas (solid grey line) compared with the Guzman–Haslam (black dashed), improved GSM (black dotted), and GMOSS (black dashed dotted) spectral index (see Section 5.1 for details). The shaded area indicates the data scatter. The combined result for dset2 alone is also shown (solid blue line) together with its standard deviation (shaded blue area).

ACKNOWLEDGEMENTS

DATA AVAILABILITY

The data underlying this article will be shared on reasonable request to the corresponding author.

REFERENCES

Anstey D., de Lera Acedo E., Handley W., 2020, preprint (arXiv:2010.09644)
Barkana R., 2018, Nature, 555, 71
Barkana R., Loeb A., 2005, ApJ, 626, 1
Benz A. O., 2009, Landolt Börnstein, 4B, 103
Bernardi G., McQuinn M., Greenhill L. J., 2015, ApJ, 799, 90
Bernardi G. et al., 2016, MNRAS, 461, 2847

Bevins H. T. J., Handley W. J., Fialkov A., de Lera Acedo E., Greenhill L. J., Price D. C., 2020, MNRAS, 502, 4405

Bowman J. D., Rogers A. E. E., Monsalve R. A., Mozdzen T. J., Mahesh N., 2018, Nature, 555, 67

Cohen A., Fialkov A., Barkana R., Lotem M., 2017, MNRAS, 472, 1915

De Oliveira-Costa A., Tegmark M., Gaensler B. M., Jonas J., Landecker T. L., Reich P., 2008, MNRAS, 388, 247

Dowell J., 2011, Parametric Model for the LWA-1 Dipole Response as a Function of Frequency. LWA Memo Series

Dowell J., Taylor G. B., Schinzel F. K., Kassim N. E., Stovall K., 2017, MNRAS, 469, 4537

Eastwood M. W. et al., 2018, AJ, 156, 32

Ellingson S. W., Craig J., Dowell J., Taylor G. B., Helmboldt J. F., 2013, 2013 IEEE International Symposium on Phased Array Systems and Technology, preprint (arXiv:1307.0697)

Fialkov A., Barkana R., Visbal E., Tseliakhovich D., Hirata C. M., 2013, MNRAS, 432, 2909

Fialkov A., Barkana R., Visbal E., 2014, Nature, 506, 197

Field G. B., 1958, Proc. IRE, 46, 240

Furlanetto S. R., Oh S. P., Briggs F. H., 2006, Phys. Rep., 433, 181

Górski K. M., Hivon E., Banday A. J., Wandelt B. D., Hansen F. K., Reinecke M., Bartelmann M., 2005, ApJ, 622, 759

Guzmán A. E., May J., Alvarez H., Maeda K., 2011, A&A, 525, A138

Harker G. J. A., Mirocha J., Burns J. O., Pritchard J. R., 2016, MNRAS, 455, 3829

Harris C. R. et al., 2020, Nature, 585, 357

Haslam C. G. T., Salter C. J., Stoffel H., Wilson W. E., 1982, A&AS, 47, 1

Hills R., Kulkarni G., Meerburg P. D., Puchwein E., 2018, Nature, 564, E32

Kocz J. et al., 2015, J. Astron. Instrum., 4, 1550003

Landecker T. L., Wielebinski R., 1970, Aust. J. Phys. Astrophys. Suppl., 16, 1

McKinley B. et al., 2018, MNRAS, 481, 5034

Mesinger A., Ferrara A., Spiegel D. S., 2013, MNRAS, 431, 621

Mesinger A., Greig B., Sobacchi E., 2016, MNRAS, 459, 2342

Mirocha J., 2014, MNRAS, 443, 1211

Mirocha J., Furlanetto S. R., 2019, MNRAS, 483, 1980

Monsalve R. A. et al., 2020, ApJ, 908, 14

Mozdzen T. J., Bowman J. D., Monsalve R. A., Rogers A. E. E., 2016, MNRAS, 455, 3890

Mozdzen T. J., Bowman J. D., Monsalve R. A., Rogers A. E. E., 2017, MNRAS, 464, 4995

Mozdzen T. J., Mahesh N., Monsalve R. A., Rogers A. E. E., Bowman J. D., 2019, MNRAS, 483, 4411

Offringa A. R., de Bruyn A. G., Biehl M., Zaroubi S., Bernardi G., Pandey V. N., 2010, MNRAS, 405, 155

Paravastu H. R. et al., 2007, Impedance Measurements of the Big Blade andFork Antennas on Ground Screensat the LWDA Site. LWA Memo Series

Patra N., Subrahmanyan R., Sethi S., Shankar N. U., Raghunathan A., 2015, ApJ, 801, 138

Philip L. et al., 2019, J. Astron. Instrum., 8, 1950004

Price D. C. et al., 2018, MNRAS, 478, 4193

Pritchard J. R., Furlanetto S. R., 2007, MNRAS, 376, 1680

Pritchard J., Loeb A., 2010, Nature, 468, 772

Rogers A., Bowman J., 2008, AJ, 136, 641

Sathyanarayana Rao M., Subrahmanyan R., Udaya Shankar N., Chluba J., 2017, AJ, 153, 26

Schinzel F. et al., 2018, A Prototype Lower-VHF Radiometry System at the Long Wavelength Array. LWA Memo Series

Schmitt H. et al., 2009, Collected LWA Engineering Memos from the Development of the Ground Screen Subsystem. LWA Memo Series

Shaver P. A., Windhorst R. A., Madau P., de Bruyn A. G., 1999, A&A, 345, 380

Sims P. H., Pober J. C., 2020, MNRAS, 492, 22

Singh S., Subrahmanyan R., 2019, ApJ, 880, 26

Singh S. et al., 2017, ApJ, 845, L12

Singh S., Subrahmanyan R., Shankar N. U., Rao M. S., Girish B. S., Raghunathan A., Somashekar R., Srivani K. S., 2018, Exp. Astron., 45, 269

Sokolowski M. et al., 2015, PASA, 32, e004

Spinelli M., Bernardi G., Santos M. G., 2019, MNRAS, 489, 4007

Tauscher K., Rapetti D., Burns J. O., 2020, ApJ, 897, 132

Taylor G. B. et al., 2012, J. Astron. Instrum., 01, 1250004

The Astropy Collaboration, 2013, A&A, 558, A33

Venkatesan A., Giroux M. L., Shull J. M., 2001, ApJ, 563, 1

Virtanen P. et al., 2020, Nature Meth., 17, 261

Voytek T. C., Natarajan A., Jáuregui García J. M., Peterson J. B., López-Cruz O., 2014, ApJ, 782, L9

Wouthuysen S. A., 1952, AJ, 57, 31

Zheng H. et al., 2016, MNRAS, 464, 3486

Zonca A., Singer L., Lenz D., Reinecke M., Rosset C., Hivon E., Gorski K., 2019, J. Open Source Softw., 4, 1298

APPENDIX A: OBSERVATION DETAILS

We detail in this appendix the total amount of hours available for

Table A1. Total hours of data analysed for antenna 254A and 252A divided in different LST slots.

LST (h)	254A (hours of data)	252A (hours of data)
0–9h	126	126
9–12h	411	321
12–24h	140	140
Total	677	587
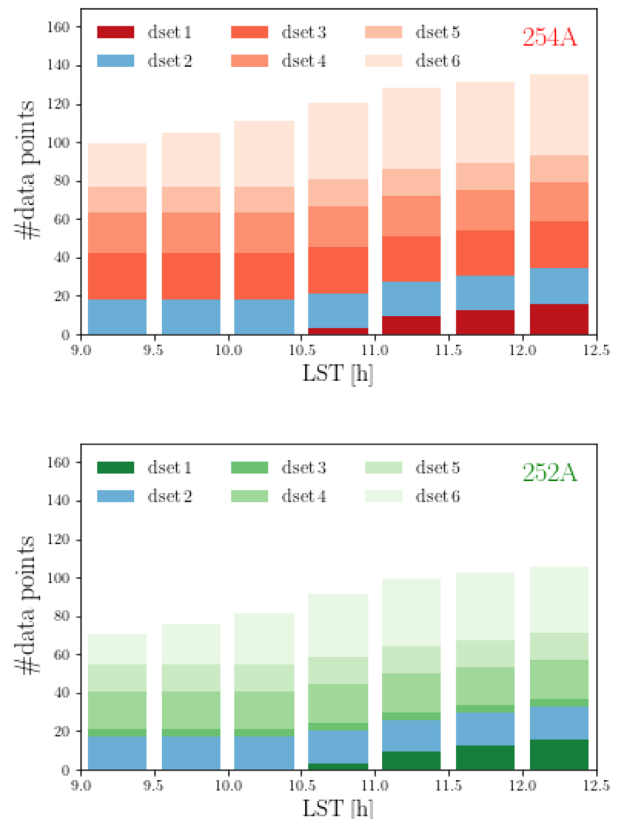
Figure A1. Total number of data points for each frequency in LST slots of ~0.5 h in the preferred 9−12.5 h LST range, for antenna 254A (top panel) and antenna 252A (bottom panel). We highlight how they are distributed between the different *data sets* following the same colour code of Fig. 5.

Table A2. Number of days observed in each data set. Note that each data set can extend beyond a calendar month.

dset	Month(s)	254A: days	252A: days
1	May2018	17	17
2 (ref)	Dec2018/Jan2019	19 (14)	17 (14)
3	Jan/Feb2019	24	12
4	Feb/Mar2019	21	20
5	Mar2019	14	14
6	Mar/Apr/May2019	42	35

our analysis. We recall that the observing season spanned from 2018 December to 2019 May. Data from 2018 May were also included. The final data set consists of 137 d of usable data. For each day, not all LST are considered. We mainly focus on the $9-12.5$ range as depicted in Fig. 3. We expand for 14 selected days in December/January the LST range to an almost 24 h LST range. We report the total amount of hours in Table A1 dividing the LST range according to this.

As discussed in Section 2, the 137 d are split in six different *data sets*. We detail the number of observing days for each of them in Table A2 and the total amount of data available per LST slot in Fig. A1. Note that the *reference* data set contains only a subset of the spectra of *dset2*, as few spectra were discarded in the analysis of the larger LST range.

APPENDIX B: STABILITY OF THE SPECTRAL INDEX RESULTS

We perform some further tests to assess the stability of our measured spectral indexes. We concentrate on results of Section 5.1, which are the central ones of this work.
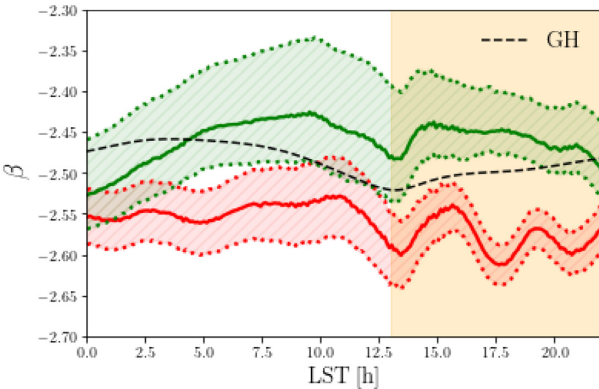
Figure B1. Mean value of the beam-corrected the best-fitting daily spectral index of Fig. 14 (254A in red and 252A in green) compared with the best fit obtained from equation 11 substituting T_{off} with $T_{off} + 1\sigma$ and $T_{off} - 1\sigma$ from Fig. 12 (dotted lines). The dashed area shows the range of spectral index values from intermediate values of T_{off}. For comparison, the Guzman–Haslam spectral index is shown (black dashed line, see equation 12). For illustrative purposes, the shaded yellow area indicates daylight, starting approximately at sunrise.
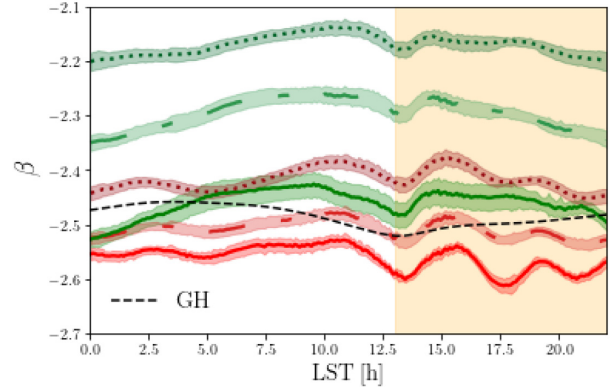
Figure B2. The mean value of the beam-corrected best-fitting daily spectral index of Fig. 14 (solid red line for antenna 254A and solid green for the 252A) compared with the best fit obtained by varying the minimum frequency considered in the fit, from the standard 60 MHz frequency to 55 MHz (dot-dashed lines) and 50 MHz (dotted lines). Red and green shaded areas show the standard deviation. The Guzman–Haslam spectral index is shown for comparison (black dashed line, see equation 12). For illustrative purposes, the shaded yellow area indicates daylight, starting approximately at sunrise.

We first investigate the dependence of our findings with respect to the offset T_{off} discussed in Section 4 and reported in Fig. 12. There is an expected correlation between the offset and the spectral index: the larger the offset that is removed, the steeper the spectral index, as the subtraction has a higher impact at high frequencies, where the sky temperature is lower. We report results obtained considering the 1σ deviation from the mean T_{off} in Fig. B1. The result for every intermediate value falls in between these solutions for both antenna 254A and 252A. The reported variations show a consistent trend with LST and deviations smaller than a few per cent for the overall spectral index value.

Our spectral index results were obtained considering a minimum frequency cut at $\nu_{min} = 60$ MHz. This choice, already discussed in Section 2, minimizes the environmental effects on the data. For completeness, we report the best fit of the spectral index for the *reference* data set obtained by lowering ν_{min} to 55 or 50 MHz in Fig. B2. We find that the spectral index tends to flatten, expected when including lower frequencies (e.g. De Oliveira-Costa et al. 2008). The effect is particularly noticeable for antenna 252A, reaching $\beta \sim -2.15$. Note, however, that the LST trend is consistent for all frequency cuts. Results for antenna 254A are more stable, as also expected from Fig. 5.

This paper has been typeset from a TEX/LATEX file prepared by the author.